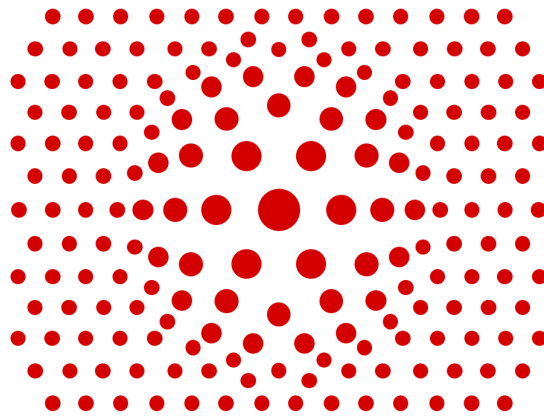




Characterization of Cell-Induced Astigmatism in Traction Force Measurements



THESIS

submitted in partial fulfillment of the
requirements for the degree of

MASTER OF SCIENCE

in

PHYSICS

Author : Rick Rodrigues de Mercado
Student ID : 1687115
Supervisor : Prof.dr. T. Schmidt
2nd corrector : Prof.dr. M.A.G.J. Orrit

Leiden, The Netherlands, February 24, 2020

Characterization of Cell-Induced Astigmatism in Traction Force Measurements

Rick Rodrigues de Mercado

Huygens-Kamerlingh Onnes Laboratory, Leiden University
P.O. Box 9500, 2300 RA Leiden, The Netherlands

February 24, 2020

Abstract

Micropillar arrays are used to measure traction forces of individual cells and of cells in tissue. For this technique single cells are placed on poly-di-methyl siloxane (PDMS) micropillar arrays and observed on an inverted high-resolution optical microscope. As of the requirements for a high-resolution inverted microscopy, the images of the micropillar array are taken through the cell. A refractive index change between the cell and cell medium results in refraction of light at their interface. Here we introduce a method to characterize astigmatism caused by this varying refractive index. We found that that astigmatism can lead to aberrations up to 400 nm. Further, based on the same method we were able to estimate the refractive index of the nucleus to be 1.366 ± 0.004 . Our results demonstrate that astigmatism should be taken into account during traction force measurements, especially when measuring forces close to the nucleus.

Contents

1	Introduction	1
2	Theory	3
2.1	Mitotic Cell as a Lens	3
3	Material and Methods	7
3.1	Cell Culture	7
3.2	Micropillar Array Preparation	7
3.3	Micropillar Stamping and Sample Preparation	8
3.4	Cell-Cycle Synchronization	10
3.5	Spinning Disk Confocal Microscope	11
3.6	Analysis	11
4	Results	15
4.1	Deflection Decomposition	15
4.2	The Deflection Field Changes Dynamically	18
4.3	Measurement Accuracy and Substrate Influence on Outward Deflections	20
4.4	The Nucleus Behaves like a Sphere-Cap Lens	24
5	Discussion	29
6	Conclusion	33
	Acknowledgements	35
	Bibliography	38
	Supplementary Information	39

Introduction

Traction force microscopy is a widely used technique to study passive cell mechanics [1, 2]. In traction force measurements, cells are placed on a soft substrate, that can be deformed by the cells. Fluorescent markers are used to measure deformation of the substrate. By doing so, information about interactions of cells with its environment are determined. Stress fields can be measured by locating fluorescent beads in an elastic substrate [3, 4]. Measuring the displacement of the beads through the substrate results in a stress field. The downside of this technique is that nearby beads are coupled through the substrate. Micropillar arrays on the other hand, are a powerful tool to measure decoupled traction forces [5]. For this technique, deflections of pillars are measured through the cell. Whilst cells are well-known to pull pillars inward due to contractility in the actomyosin network [6], previous studies using super-resolution techniques on micropillar arrays have also measured pushing forces in nN range during cell division [7, 8].

Traction force measurements on micropillar arrays image the position of pillar-tips through the cells. The refractive indices of the cell and its surrounding medium is not the same, and even within cells the refractive index is not constant [9]. This refractive index change opposes the problem that light can be refracted at the interface between the cell and the cell-medium. This refraction might result in an untrue measurement of pillar positions. Incorrect interpretation of micropillar deflections leads to wrong conclusions.

In this thesis, we introduce a method to determine cell-induced astigmatism during traction force measurements on micropillar arrays. Using μ -contact printing, we printed a repetitive pattern on a stiff flat layer of poly-di-methyl siloxane (PDMS). The layer was too stiff for the cells to be

able to deform the pattern. Hence, any deformations observed on this flat layer are the result of astigmatism. We use this method to characterize astigmatism caused by the cell-nucleus. Further, we introduce a simple model that explains the observed deformations of the substrate due to the lens effect. We assume that the shape of the nucleus is similar to a sphere-cap and calculated aberrations caused by refraction of light at the curved surface.

We found that when we imaged HeLa cells on this nondeformable pattern, we nonetheless observed deformations of the pattern. We compared these deformations to measurements of (dividing) cells on micropillar arrays. The stiffness of the micropillars influenced the size of the deflections, probably because cell-behaviour was affected by the environment. Lower outward deflections were observed on soft micropillars compared to stiff pillars.

For HeLa cells during metaphase, similar outward deflections were found on stiff 47.2 kPa micropillars as well as on a pillar-spot printed 2.5 MPa flat layer. The size of deflections increased from 0 nm at the center of the nucleus toward up to 400 nm at its edge, which is equivalent to traction forces in nN range. Pillars/pillar-spots surrounding the nucleus showed decreasing deflections as the distance to the center increased. These results indicate that astigmatism was the main cause of pushing forces measured previously [8]. Further, based on our model we found an estimation for the refractive index n of the nucleus: $n = 1.366 \pm 0.004$.

The model introduced in this thesis does not explain why deflections of pillars surrounding the nucleus showed a downward trend, since it does not differentiate between the nucleus and the cytosol. The question remains how this downward trend can be explained.

Theory

The principle of a lens originates from a difference in refractive index between two media. At the interface between the media, light gets refracted. The curvature of this interface and the refractive index difference determine the strength of the lens. Because of the optical techniques used to image biological cells, these cells could qualify as a lenses since they meet these requirements. First of all, nuclei of cells have a different refractive index than their surrounding [9]. Furthermore, during the cell cycle of mitotic animal cells, the shape of the cells changes considerably from flat to round [10]. The combination of these two make the cell a potential lens, especially during cell division. Here, we present a simple model to calculate astigmatism due to refraction of light at the interface between the nucleus and its surrounding.

2.1 Mitotic Cell as a Lens

As an approximation, we model the nucleus as a sphere-cap of radius R of which a height $H \leq 2R$ is above the surface of a substrate. The light emitted by a fluorescent label on the substrate is assumed to exit the nucleus perpendicular to the substrate. Figure 2.1 shows a projection of the sphere in 2D. The sphere is placed in a medium with refractive index n_1 . The sphere itself has refractive index n_2 . A light ray (red in figure 2.1) is gets refracted at interface between the medium and the sphere. Due to the refraction, a net shift Δx is observed. To find the analytical expression of this shift, we start by relating the angle of refraction of the ray to the

position it reaches the sphere:

$$\sin \theta_1 = \frac{x'}{R} \quad (2.1)$$

Where θ_1 is the angle of refraction at position x' .

Using Snell's law we can find an expression for the incident angle θ_2 in terms of geometrical constants:

$$\sin \theta_2 = \frac{n_1}{n_2} \sin \theta_1 = \frac{n_1 x'}{n_2 R} \quad (2.2)$$

The difference Δx between the observed position x' and the real position x is:

$$\frac{\Delta x}{R} = \frac{x' - x}{R} = \frac{h}{R} \tan(\theta_1 - \theta_2) \quad (2.3)$$

Where h is the height of the sphere at position x' .

We define a length $L = h + R - H$. We can make a right triangle $\triangle Rx'L$ such that $L^2 = R^2 - x'^2$. An expression for h/R can then be found:

$$\left. \begin{array}{l} \frac{L}{R} = \frac{1}{R} \sqrt{R^2 - x'^2} = \sqrt{1 - \frac{x'^2}{R^2}} \\ L = h + R - H \end{array} \right\} \frac{h}{R} = \sqrt{1 - \frac{x'^2}{R^2}} - \left(1 - \frac{H}{R}\right) \quad (2.4)$$

Then, combining eq. 2.3 and eq. 2.4 results in:

$$\frac{\Delta x}{R} = \left[\sqrt{1 - \left(\frac{x'}{R}\right)^2} - \left(1 - \frac{H}{R}\right) \right] \tan(\theta_1 - \theta_2) \quad (2.5)$$

Combining eq. 2.1, eq. 2.2 and eq. 2.5 results in the final expression for the pseudo-deflection Δx :

$$\Delta x = R \left[\sqrt{1 - \left(\frac{x'}{R}\right)^2} - \left(1 - \frac{H}{R}\right) \right] \tan \left(\arcsin \frac{x'}{R} - \arcsin \frac{n_1 x'}{n_2 R} \right) \quad (2.6)$$

Which, as a function of x' , in the end only depends on the radius of the sphere R , the height H that is above the surface, and the refractive indices of the medium n_1 and the sphere n_2 .

Of course, light is not emitted in a single direction. Figure 2.2 A shows another beam of light (blue) emitted by the substrate that is directed perpendicular to the substrate. With a similar derivation as for eq. 2.6, the

following expression for the pseudo-deflection is obtained for this light path:

$$\Delta x = R \left[\sqrt{1 - \left(\frac{x}{R}\right)^2} - \left(1 - \frac{H}{R}\right) \right] \tan \left(\arcsin \frac{n_2 x}{n_1 R} - \arcsin \frac{x}{R} \right) \quad (2.7)$$

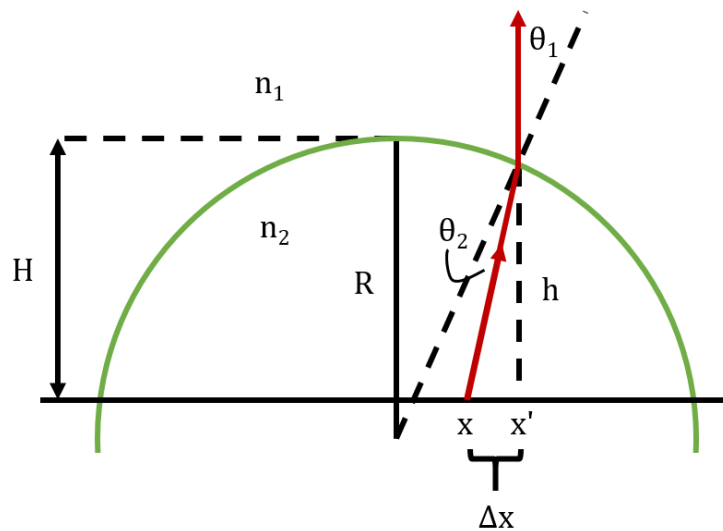


Figure 2.1: Refraction at a spherical surface results in a shift Δx between the real pillar position x and the observed pillar position x' . A light ray (red) is shown for the case that $n_2 > n_1$.

Figure 2.2 B shows the function of eq 2.6 and eq 2.7 in the case that $R = 10 \mu\text{m}$, $H = 10 \mu\text{m}$, $n_1 = 1.33$ and $n_2 = 1.38$. For distances close to the center, the curvature of the sphere is almost parallel to the substrate. There, the difference between the incident and outgoing angle is small, hence deflections are small. Deflection initially increase linearly as the distance from the center increases. The angle at which the light is emitted has little influence on the slope of this linear regime. When the curvature becomes more perpendicular to the substrate, the deflection caused by the two modelled curves deviate. A maximum is reached close to the edge of the sphere. In the case of the parameters that were used, deflections can be up to 300-700 nm.

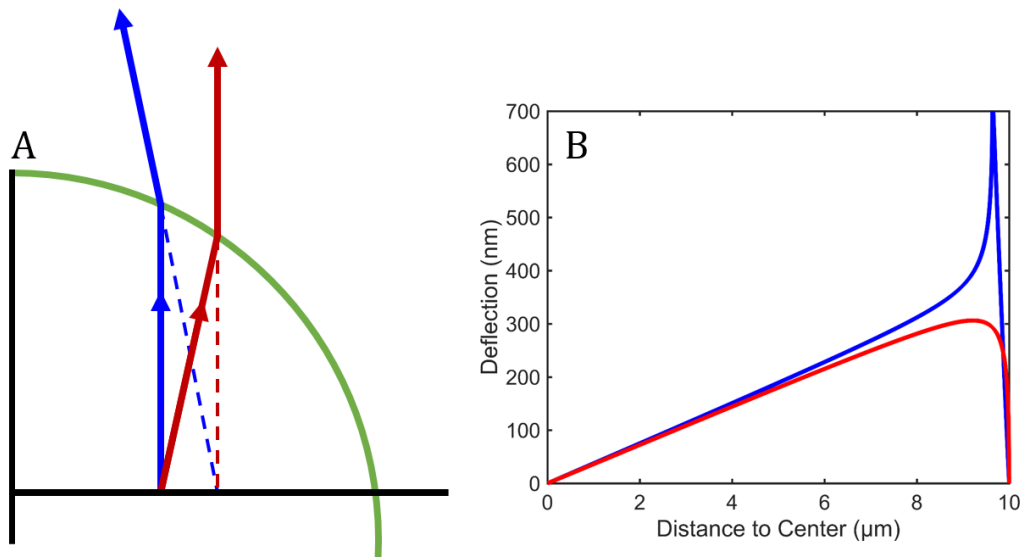


Figure 2.2: Lensing effect is maximum near the edge of the nucleus. **A.** Light paths resulting in eq. 2.6 (red) and eq. 2.7 (blue). Light is emitted in different directions by the fluorescent labels on the substrate. The angle of emission influences the amount of astigmatism. **B.** Function of eq. 2.6 (red) and eq. 2.7 (blue) for $R = 10 \mu\text{m}$, $H = 10 \mu\text{m}$, $n_1 = 1.33$ and $n_2 = 1.38$. Deflections due to lensing initially have the same slope, independent of the emission angle. Near the boundary of the nucleus, the emission angle plays a significant role. Close to the edge, deflections are up to 300 - 700 nm.

Material and Methods

HeLa cells were used to measure deflections of poly-di-methyl siloxane (PMDS) micropillars during cell division. Astigmatism was quantified by measuring deformations of a hexagonal pattern caused by dividing cells on an undefinable flat layer of PDMS.

3.1 Cell Culture

HeLa cells expressing H2B-GFP (488 nm) were cultured in high-glucose Dulbecco's Modified Eagle's Medium (DMEM) supplemented with 10 % fetal calf serum (Thermo Scientific), 2 mM glutamine and 100 $\mu\text{g mL}^{-1}$ penicillin/ streptomycin at 37 °C with 5 % CO₂.

3.2 Micropillar Array Preparation

Micropillar arrays were made of poly-di-methyl siloxane (PMDS) [11, 12]. Liquid PDMS was poured onto a silicon wafer, which was either flat or contained the negative mold of the micropillar arrays. Micropillars were located on the nodes of a hexagonal lattice, had a width of 2 μm and a center-to-center distance of 4 μm . Two different kind of micropillars were used which we differentiate based on their Young's modulus: soft 9.8 kPa pillars (6.9 μm height) and stiff 47.2 kPa pillars (4.1 μm height). During measurement, the micropillar arrays were flipped upside down. To prevent cells from getting crushed between the array and the glass coverslip, there were 50 μm spacers on two sides of the array (figure 3.1). The following steps were performed to make the micropillar arrays:

1. PDMS (Sylgard 184 Silicone Elastomer kit) base and crosslinker were mixed thoroughly in a ratio of 10:1;
2. The PMDS mixture was degassed at 150 mbar for 1 h to remove air bubbles;
3. The PDMS was poured onto the silicon wafer and degassed again for 30 min to remove any air bubbles due to transfer of the liquid;
4. When all air bubble were gone, the wafer was cured in the oven for 20 h at 110 °C;
5. The micropillar arrays were carefully peeled of the wafer and stored;
6. The wafer was cleaned with isoproponol twice and dried for 30 min at 65 °C;
7. The wafer was silanized for 2 h at 150 mbar and stored for re-use;

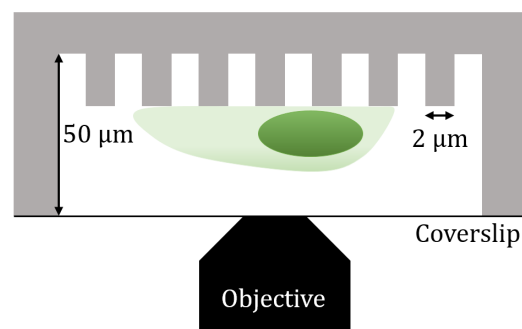


Figure 3.1: Schematic overview of a micropillar array in the upside down position on top of the inverted spinning disk setup.

3.3 Micropillar Stamping and Sample Preparation

Fibronectin (Sigma-Aldrich, F1141) labelled with Alexa-568 dye was used to coat the tops of the micropillars. A soft PDMS stamp (base:crosslinker = 30:1) was used to cover the tips of the micropillars with fibronectin. To ensure cells only attached to the tops of the micropillars, the sides of the pillars were covered with pluronic (Sigma-Aldrich, F127). Micropillar

arrays are used to measure traction forces exerted by cells. A stiff flat layer of PDMS (base:crosslinker = 10:1) was used to quantify the astigmatism caused by the cell. An undeformable hexagonal pillar-pattern was printed on top of the flat layer. Measured deformation of the pattern on this layer then solely resulted from refraction of light.

The following steps were performed to print fibronectin on top of the pillars:

1. Unlabelled and Alexa-568-labelled fibronectin were mixed in a ratio 5:1 and diluted in water to 60 $\mu\text{g}/\text{mL}$ fibronectin;
2. A 40 μL drop was placed on top of the stamp for 1 h;
3. The stamp was flushed with water and subsequently dried for 25 min;
4. Meanwhile, a micropillar array was activated with UV-Ozone for 10 min;
5. The dried stamp was placed on top of array for 10 min;
6. 100 % ethanol was added and the stamp was removed;
7. The 100 % ethanol was aspirated and the array was flushed with 70 % ethanol;
8. Subsequently the array was incubated for 1 h in 0.2 % pluronic in phosphate buffered saline (PBS);
9. The pluronic was aspirated and the micropillar array was flushed three times with PBS;
10. The micropillar array was stored in PBS at 4 $^{\circ}\text{C}$ up to two days;

Stamping of the hexagonal micropillar pattern on a flat layer of PDMS was similar to stamping of the real micropillars. The difference is that after step 5 the stamp was removed without being submerged in 100 % ethanol. The micropillar array was then placed on top of a flat layer of PDMS for 10 min, which was also activated for 10 min with UV-Ozone. Then steps 6-10 were completed as above. Figure 3.2 shows a schematic picture of this two-step stamping method. A visual comparison between direct μ -contact printing on a micropillar array, and the two-step stamping method on a flat layer is shown in figure 3.3.

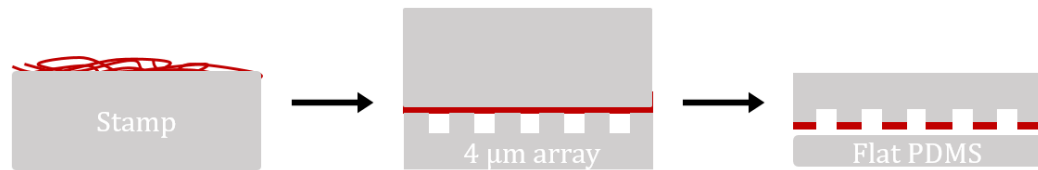


Figure 3.2: A schematic overview of the two-step stamping method. A soft PDMS-stamp was covered with fluorescently labelled fibronectin and placed on top of a micropillar array. After incubation, the stamp was removed and the micropillar array was placed on top of a flat layer of PDMS to transfer the pillar-pattern.

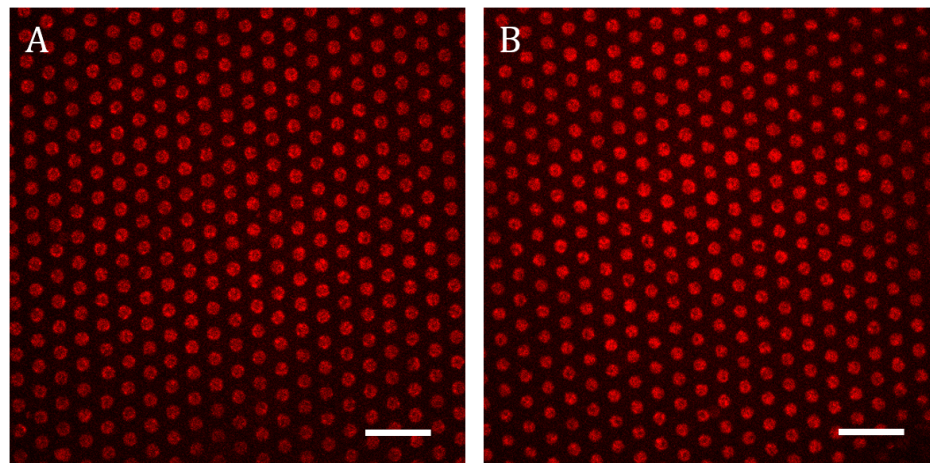


Figure 3.3: Result of μ -contact printing of fibronectin on a micropillar array (A) and through the two-step stamping method on flat layer of PDMS (B). The scalebar in the lower right is $10 \mu\text{m}$.

3.4 Cell-Cycle Synchronization

The probability of measuring a successful cell division was increased by the use of RO3306 (Sigma-Aldrich, SML0569). This inhibitor was added to the cells in a final concentration of $10 \mu\text{M}$ in cell medium before they were transferred to the micropillar array. RO3306 synchronizes HeLa cells in late G2 phase [13]. RO3306 is an inhibitor of the CDK1 complex and prevents cells from proceeding into mitosis. HeLa cells were added on top of the micropillar array, such that they had a surface coverage of $\sim 5 \cdot 10^3 \text{ cells/cm}^2$. After an incubation of 16-20 h on top of the pillars, the inhibitor was removed by flushing the micropillar array twice with PBS.

Then, the micropillar array was placed in cell medium. After releasing the cells from the RO3306 block, about 20 - 30 % of the cells rapidly proceeded through mitosis. Measurement were done shortly after the release.

3.5 Spinning Disk Confocal Microscope

A home build inverted spinning disk confocal high-resolution microscope was used to measure traction forces of HeLa cells during cell division. The main body of the microscope consisted of an Axiovert200 (Zeiss) with a 100x 1.40 NA oil objective (Zeiss). Confocal imaging was achieved by means of a spinning disk unit (CSU-X1, Yokogawa). Images were recorded with an emCCD camera (iXon 897, Andor). Tailor made software (Labview, National Instruments) was used to control a home-build auto-focus system and an automated translation stage (Marzhauser XY-stage). Excitation of the fluorescent labels was achieved by lasers of wavelength 488 and 561 nm (Coherent and Cobolt respectively). Life cell measurements were performed in a stage-top incubator (Tokai Hit) at a constant temperature of 37 °C and 5 % CO₂.

3.6 Analysis

The main analysis was done in Matlab (2017a). Traction forces exerted by HeLa cells on micropillars were calculated by comparing the deflection of each pillar to a reference grid. A two dimensional Gaussian was fit to the circular spots of individual micropillars. From this fit, the center of each pillar was determined with an accuracy up to 10-20 nm. A reference grid was created by calculating the nearest-neighbour distance for each pillar. The pillar deflections were calculated by comparing the fitted pillar-center to the reference grid, as shown in figure 3.4.

Allocating pillars to the nucleus or the cell was done by means of a threshold function as shown in figure 3.5. The threshold was applied to the GFP channel (marking histone H2B), which masks the nucleus. The center of mass of the threshold-mask was used as the center of the nucleus. The size of the cell itself was not known and could not be determined via measurements, since the cytosol did not contain any fluorescent markers. For the cell-mask, a 10 µm ring was added on all sides of the mask of the nucleus to ensure most of the pillars underneath the cell were included. In the end, all pillars underneath the mask were assigned to the cell as shown in figure 3.5 D.

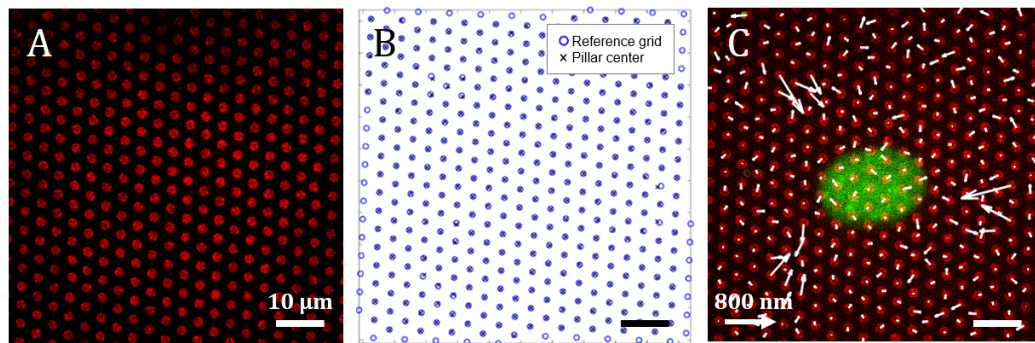


Figure 3.4: Micropillar deflections were determined by comparing the center-points of the pillars to a reference grid. **A.** Image of a micropillar array. The pillar tips were coated with fluorescently labelled fibronectin (red, Alexa 568). Pillar positions were determined by using a threshold. For each pillar detection, a two dimensional Gaussian was fit to determine its center-point. **B.** Reference grid and pillar center-points resulting from the fit. **C.** Image of micropillars and a nucleus (green, H2B-GFP) of a HeLa cell. The deflection of each pillar is shown by a white arrow. The scalebar in the lower right is consistent for all images.

Deflection found by eq. 2.6 are in the direction radially away from the center of the sphere-cap. To compare measured deflections with this simple model, deflections were separated into a radial and tangential component with respect to the center of the nucleus as shown in figure 3.6. After verification (section 4.1), tangential components were discarded and further calculations were done with radial components only.

Significance between two conditions was determined via the Wilcoxon rank sum test. Errors in fit-results indicate a 95 % confidence bounds.

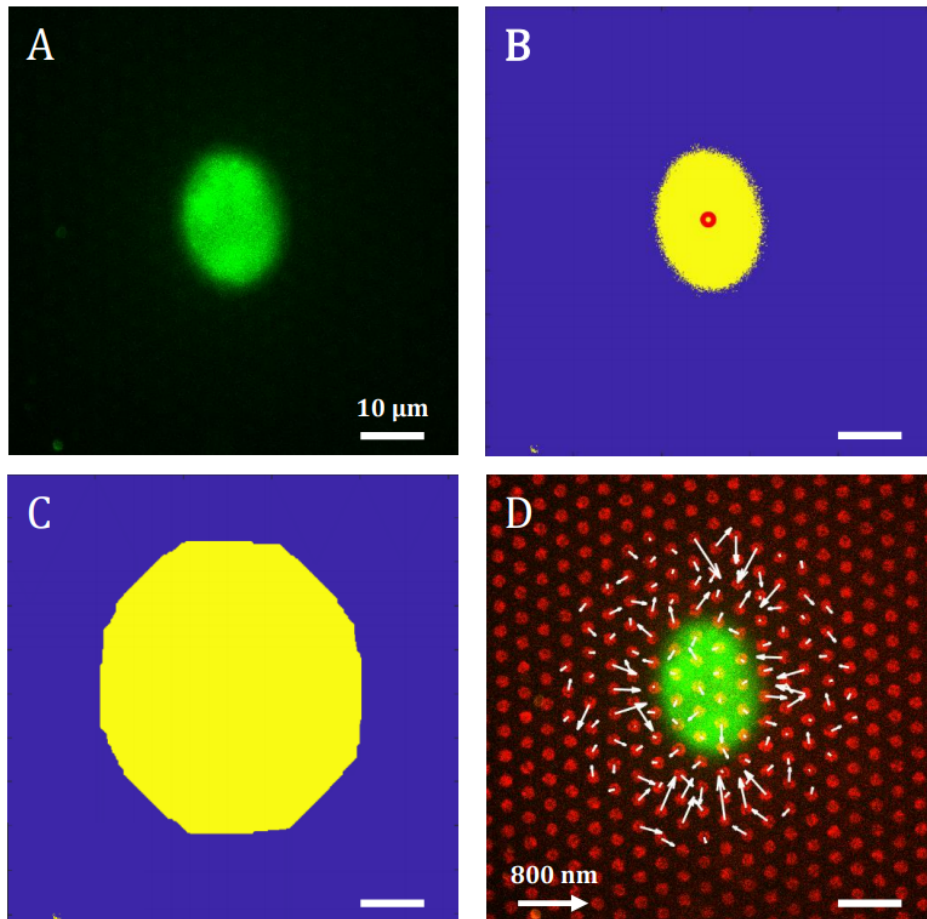


Figure 3.5: A threshold function was used to determine the center of the nucleus and to select the pillars underneath the cell. **A.** The nucleus of a HeLa cell (H2B-GFP) on top of micropillars (not shown). **B.** Threshold image of (A). The center of the nucleus (red circle) was determined by the center of mass of this threshold. In each image, this center was manually selected. **C.** Extrapolation of the threshold shown in (B). The size of the mask is chosen such that it covers most of the cell. **D.** Deflection field that follows from the reference grid analysis for the pillars (red, Alexa 568) underneath the cell-mask. The nucleus is shown in green. Deflection scalebar is in the bottom left. Fluorescent scalebar in the lower right is consistent for all images.

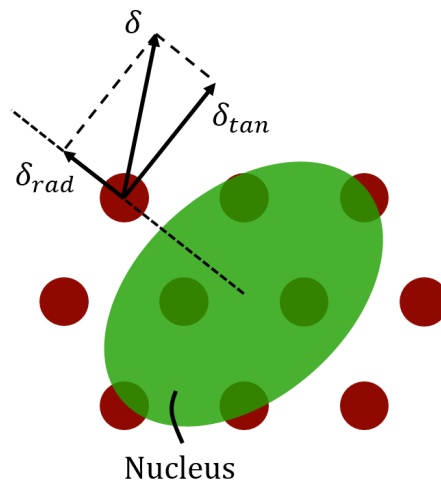


Figure 3.6: Deflections δ can be separated into radial δ_{rad} and tangential δ_{tan} components with respect to the center of the nucleus.

Results

HeLa cells were used to quantify cell-induced astigmatism during traction force measurements. Measurements were performed on three different substrates: soft 9.8 kPa micropillars, stiff 47.2 kPa micropillars and a stiff 2.5 MPa flat layer of PDMS. Deflections of pillar-spots were split into radial and tangential component with respect to the center of the nucleus. The highest outward pointing deflections were observed during metaphase. Eq. 2.6 was used to determine an indication of the relative refractive index change between the nucleus and its surrounding that causes the refraction during metaphase.

4.1 Deflection Decomposition

Deflections of pillar-spots were separated into radial and tangential component with respect to the center of the nucleus. Underneath and around the nucleus of a metaphase cell, clear outward pointing deflections were observed (Fig. 4.1 A). The median of the full absolute deflection field as shown in figure 4.1 A-B was 44 ± 4 nm (median \pm SEM). This value was set as a lower bound in determining pillar deflections in this field of view, i.e. deflections that were much larger than 44 nm were caused by external influences and were not limited by our measurement accuracy.

Decomposition of the deflections into radial and tangential component with respect to the center of the nucleus is shown in figure 4.1 C, E respectively. This was done only for the deflections of pillars within the cell-mask (i.e. in general all pillars within ~ 20 μm of the center of the nucleus), which was big enough to capture all pillars underneath the cell. A larger amount and bigger outward pointing (positive) radial deflections

were observed compared to inward pointing (negative) radial deflections (Fig. 4.1 D). The tangential components of the deflections were distributed around zero (Fig. 4.1 F). Here, clockwise was defined as positive, anticlockwise as negative. In this case, but also in general, the distribution of tangential deflection was much narrower than the distribution of radial components. The distribution of radial components had a median of 20 nm, and a standard deviation of 111 nm. This distribution was not centered around zero, but shifted towards more positive deflections with positive deflections up to 400 nm. The distribution of tangential components on the other hand had a median of 4 nm, with a standard deviation of 44 nm. This distribution was centered at zero, and had most deflections

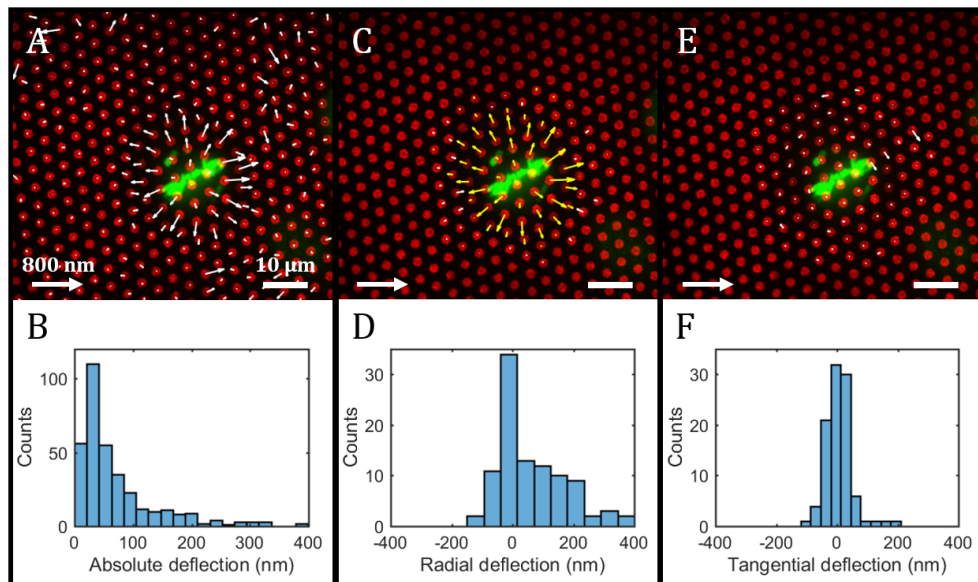


Figure 4.1: Decomposition of deflections resulted in a net outward radial deflection, while the distribution of tangential components was centered at zero. **A-B.** Full deflection field around a metaphase cell on a 9.8 MPa micropillar array (red, Alexa 568). The nucleus of a metaphase HeLa cell is shown in green (H2B-GFP). The deflection of each pillar is shown by an arrow. **C-D.** Radial component of deflections of pillars within the cell-mask. Deflection facing away (positive deflection) from the center of the nucleus are displayed in yellow. Pillar deflections towards (negative deflection) the center of the nucleus are displayed in white. **E-F.** Tangential component of deflections of pillars within the cell-mask. Clockwise is defined as positive, anticlockwise as negative. The deflection scalebar in the lower left and fluorescent scalebar in the lower right are consistent for each image.

within the regime of high measurement inaccuracy. Considering the absolute value of the radial deflections, the distribution had a mean of 88 ± 9 nm (mean \pm SEM); a factor of two above the measurement threshold. The distribution of absolute tangential deflections had a mean of 31 ± 3 nm (mean \pm SEM), which is below the lower bound previously defined.

Ultimately, we want to use just the radial component of the deflections to quantify the lens effect, because eq. 2.6 and 2.7 calculate the deflection in the radial direction only. We tested the dependency of the net tangential deflection on the substrate stiffness (which changes cell behaviour [14]) and shape changes of the cell. To calculate the net tangential deflection, all tangential components of deflections of the pillars/pillar-spots in the cell-mask were added together. The results are shown in figure 4.2. We compared the deflection fields of 70 interphase and 11 metaphase cells on soft micropillars, 65 interphase and 19 metaphase cells on stiff micropillars, and 49 interphase and 16 metaphase cells on a stiff flat layer of PDMS. We found that net tangential deflections were independent of the type of substrate, and the phase of the cell. For each distinct case, the net tangential deflections were distributed around zero. All p-values were above 0.25 (Table S1).

The lack of information in the (net) tangential component indicates that the radial component of the deflections is sufficient to quantify the astigmatism caused by the cell.

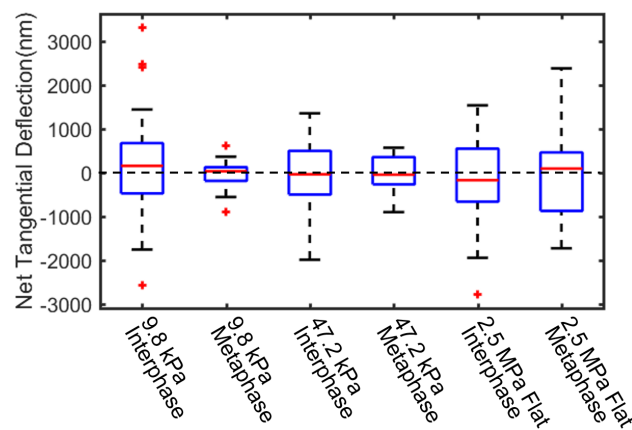


Figure 4.2: The net tangential deflection of single cells is independent of the stiffness of the substrate and phase of the cell. Each distribution of net tangential deflections is not significantly different from any other distribution. From left to right, the number of data points per boxplot is 70, 11, 65, 19, 49, 16.

4.2 The Deflection Field Changes Dynamically

During cell division, forces exerted by cells on their environment change dynamically [8]. A time series measurement on single cells gives insight in these changes. Figure 4.3 A-C shows snapshots of such time series. It shows the nucleus of a HeLa cell on a stiff micropillar array. Clear changes in the radial component of the deflection field of the micropillars were observed. Initially during interphase (Fig. 4.3 A), the nucleus (and cell) was spread over the micropillars and the cell exerted large traction forces on some pillars. While the cell rounded up during metaphase (Fig. 4.3 B) [10], we saw that pillars close to the nucleus were deflected outward more. During metaphase, we observed a peak-plateau in the net radial deflection (Fig. 4.3 D) between 470 and 520 min. The net radial deflection was calculated by summing all radial components of the deflections together, taking outward pointing deflections as positive and inward pointing deflections as negative. Shortly after DNA separation at 520 min, we still observed outward deflections close to the nucleus. The cell then started spreading over the substrate while we saw a gradual decrease in the net radial deflection and the re-appearance of larger traction forces (Fig. 4.3 C).

The shape change from flat to round (and back) we modelled by linearly changing the shape of a sphere-cap to mimic cell-rounding during mitosis. The volume and refractive index of the sphere-cap were assumed to be constant. Based on eq. 2.6, deflections were calculated and averaged over the area covered by the sphere-cap (green line in figure 4.3 D). For the interphase (< 425 min), typical observed values (not in this thesis) were used; $H = 8.8 \mu\text{m}$, $R = 12.6 \mu\text{m}$. Between 425 min and 475 min, the cell was assumed to transition linearly from this state to the metaphase, where $H = 9.4 \mu\text{m}$, $R = 8.6 \mu\text{m}$ (see section 4.4). An increase in the mean deflection was observed during this transition. This configuration was conserved for 35 min, resulting in a peak-plateau. The sphere-cap changed from round to flat again between 510 and 540 min, during which the mean deflection decreased. The change in mean deflection for this simple shape change is similar to the change in net radial deflection which was observed during cell division.

Cell rounding during metaphase results in an increase in net radial deflections.

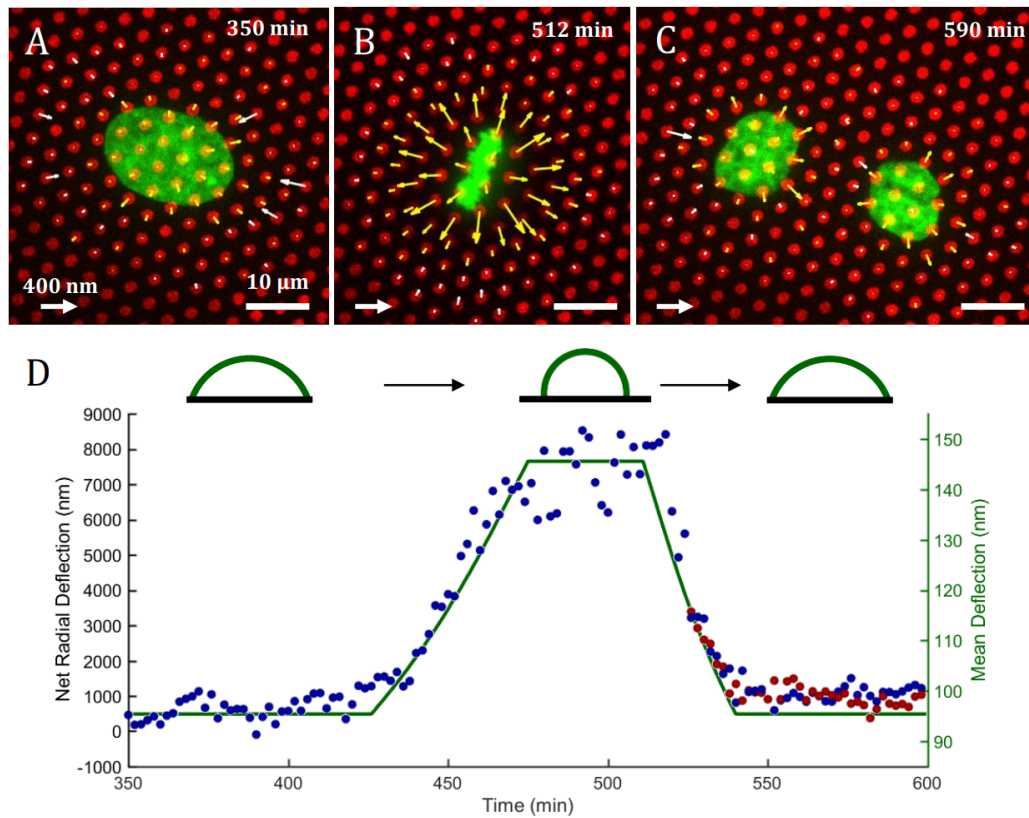


Figure 4.3: The net radial deflection is highest during metaphase. **A.** A HeLa cell during interphase on a 47.2 kPa micropillar array. The radial deflection of each pillar is shown by an arrow. We see the cell pulling pillars inward (white). Outward deflections are displayed in yellow. **B.** The same cell during metaphase. Traction forces had vanished. Within the cell-mask, we saw pillars deflected outward. **C.** After cell division, the cells had spread over the substrate and exerted traction forces on the pillars again. **D.** Time series of the net radial deflection during cell division. The net radial deflection had a peak-plateau during metaphase at around 500 min. After cell division (split into red and blue for each individual cell) the net radial deflection gradually decreased. In green, the mean deflection caused by a modelled cell transitioning from flat to round and back is shown based on eq. 2.6. The deflection scalebar in the lower left and fluorescent scalebar in the lower right are consistent for each image. (Data: M. De Valois)

4.3 Measurement Accuracy and Substrate Influence on Outward Deflections

The significant change in the radial deflections during metaphase was observed on all substrates. In figure 4.4 we see metaphase cell on both the soft and stiff micropillars, as well as on the stiff flat layer of PDMS. In each image, we see pillars underneath and around the nucleus deflected outward. The flat layer of PDMS was too stiff for the cell to deform the pillar-spots. The measured deflections on the flat layer were therefore solely due to refraction of light by the cell.

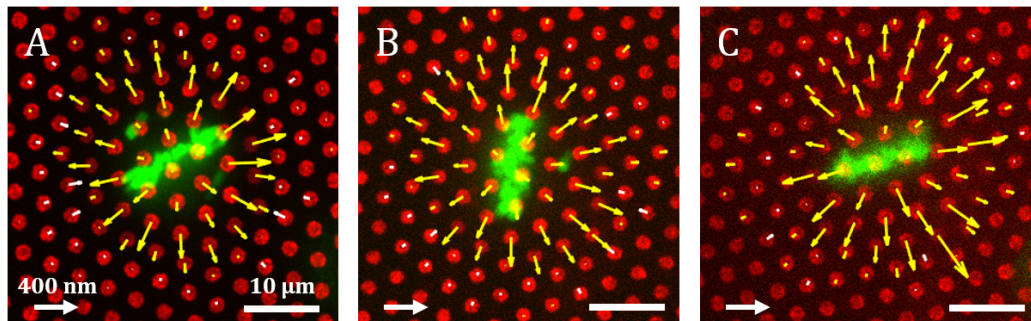


Figure 4.4: Visual comparison of radial deflection fields of metaphase cells on 9.8 kPa pillars (A), 47.2 kPa pillars (B) and 2.5 MPa flat layer (C). The displacement of the pillar-spots (red, Alexa 568) around the nucleus (green, H2B-GFP) is shown by arrows. Similar outward pointing deflections (yellow) are observed for each substrate. Inward pointing deflections are shown in white. The deflection scalebar in the lower left and fluorescent scalebar in the lower right are consistent for each image.

For each substrate, we compared the deflection field of the whole field of view as in figure 4.1 A-B. This gives an indication of the measurement accuracy we can achieve on each substrate. The distributions of all absolute deflections are shown in figure 4.5. In total 81, 84 and 65 field of views (each field of view consists of 300 - 350 pillars) were used for the 9.8 kPa pillars, 47.2 kPa pillars and 2.5 MPa flat layer respectively. The soft and stiff micropillars had a similar accuracy, as would be expected since they were prepared in exactly the same way. Their distributions have a median of 83 and 84 nm respectively. The distribution on the flat layer of PDMS on the other hand, showed a median of 113 nm, much higher compared to the micropillar arrays. During the double stamping method, the (fluorescently labelled) fibronectin was transferred from the cube to the flat

PDMS layer by using a micropillar array. During this procedure, not all fibronectin was transferred from the array to the flat layer. The pillar-spots on the flat layer were covered by less fibronectin compared the the tops of the pillars themselves resulting in less photons being released after excitation of the fluorophores on the flat layer.

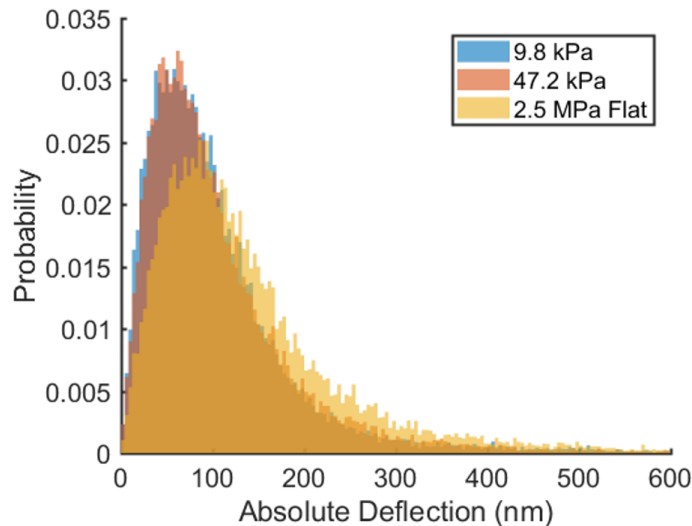


Figure 4.5: During the double stamping method, some fluorescent signal is lost resulting in a lower measurement accuracy on the flat PDMS layer. Normalized absolute deflection distribution of 81, 84, 65 field of views (300 - 350 pillars) on 9.8 kPa pillars, 47.2 kPa pillars and 2.5 MPa flat layer respectively. Their respective medians are 83 nm, 84 nm and 113 nm.

The influence of the measurement accuracy on the radial component of the deflections was also tested. In total 11, 19 and 16 regions underneath and surrounding metaphase cells (~ 45 pillars per region) were used for the 9.8 kPa pillars, 47.2 kPa pillars and 2.5 MPa flat layer respectively. Figure 4.6 shows the distributions of radial deflection for these three substrates. Radial deflections on stiff micropillars and stiff flat PDMS layers showed similar distributions. Both showed outward pointing deflections of which the distributions had medians 161 and 158 nm respectively. A few negative deflections were measured on the flat layer of PDMS. These deflections mainly resulted from incorrect pillar detections due to the lower pillar-spot brightness. Radial deflections on the soft micropillars were closer to zero compared to the two stiffer substrates, but pillars were still deflected outward. This distribution had a median of 78 nm. Hence, there was in total less fibronectin for the cell to adhere to due to the dou-

ble stamping method [14], but the radial deflections were of same size nonetheless.

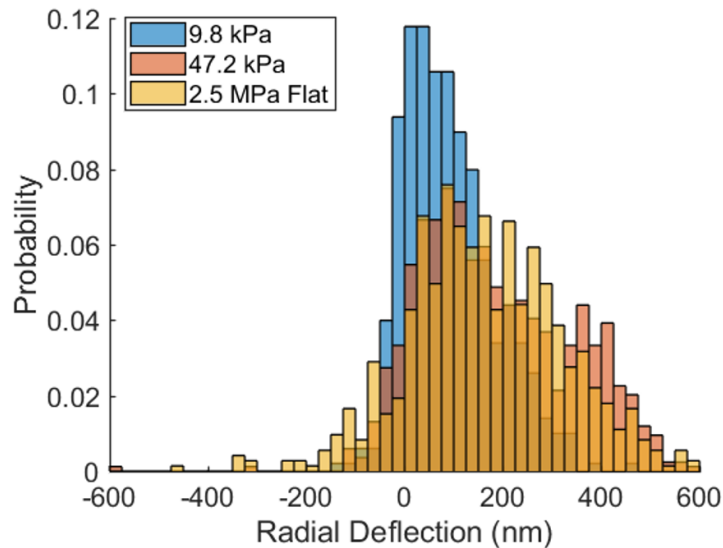


Figure 4.6: Radial deflections of pillars within the cell-mask of metaphase cells are independent of the measurement accuracy, but are influenced by the stiffness of the substrate. Normalized radial deflection distribution of 11, 19, 16 regions underneath metaphase cells (~ 45 pillars per region) on 9.8 kPa pillars, 47.2 kPa pillars and 2.5 MPa flat layer respectively. Their respective medians are 78 nm, 161 nm and 158 nm.

More quantitatively, we calculated the net radial deflection per cell. We summed all radial components of the deflections of pillars within the cell-mask. We did this for 70 interphase and 11 metaphase cells on soft pillars, 65 interphase and 19 metaphase cells on stiff pillars, and 49 interphase and 16 metaphase cells on a stiff flat layer of PDMS. The results are shown in figure 4.7. We saw that on each substrate the net radial deflections were higher during metaphase than during interphase. Most cells on the soft micropillars in interphase showed negative net radial deflections. These cells were spread out over the substrate and exerted traction forces on the pillars near the cell edges. Interphase cells on stiff micropillars showed less of these traction forces. We saw, on average, a higher net radial deflection for these cells compared to interphase cell on soft pillars. Interphase cells on the flat layer of PDMS showed similar values for the net radial deflection. Here deflections were not caused by the cell deforming the substrate, but only by astigmatism induced by the cell.

A similar trend was observed for metaphase cells on the three substrates. On the soft micropillars, cells had on average the lowest net radial deflections. The net deflections on the stiff pillars and flat layers again showed similar values. All p-values are shown in supplementary information table S2. Resulting p-values above 0.05 are displayed as *ns* in figure 4.7. Most interesting is that the distributions of net radial deflection on stiff micropillars was similar to those on a flat layer of PDMS, indicating that cells did not push the stiff pillars during cell division. The observed deflections were caused by a lens-effect.

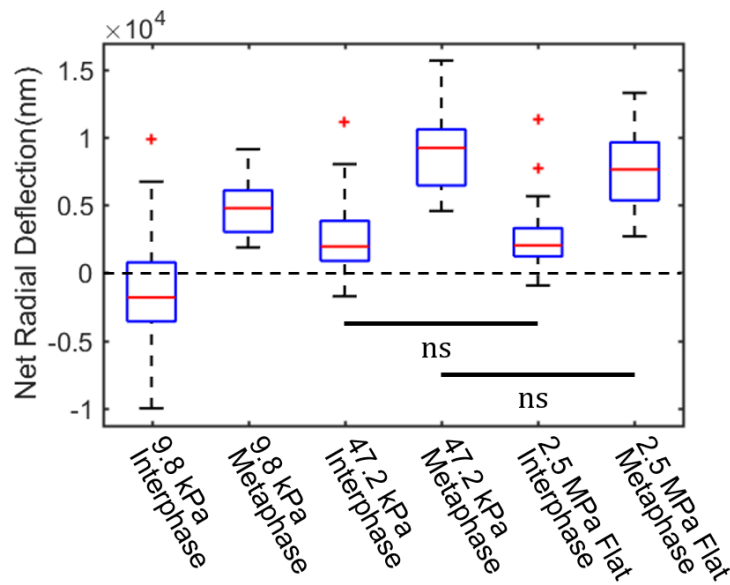


Figure 4.7: The net radial deflection of cells on a flat layer of PDMS shows no significant difference to the summed radial deflection on stiff micropillars. On each substrate, the net radial deflection was higher during metaphase than during interphase. The size of the radial deflections depend on the stiffness of the substrate. From left to right, the number of data points per boxplot is 70, 11, 65, 19, 49, 16.

The size of outward deflections depends on the stiffness of the substrate. The 47.2 kPa micropillars were too stiff for the cells to bend. Deflections measured on these arrays were the result of astigmatism.

4.4 The Nucleus Behaves like a Sphere-Cap Lens

Until now, deflections were compared without taking into account the distance of their respective pillars to the (center of the) nucleus. We want to find the relation between the distance of a pillar/pillar-spot to the center of the nucleus and the deflection of the spot and compare it to figure 2.2. Interphase cells did not show a clear correlation between the pillar-to-center distance and the deflection (Fig. S1). During metaphase, DNA inside the cells formed an elliptical shape. The threshold function (explained previously in section 3.6) returned values for the semi-short and semi-long axis of this ellipse. The radius of the nucleus R_{nuc} was determined by taking the average of the two. Depending on the distance d to the center of the nucleus, we can differentiate two regimes:

1. $d < R_{nuc}$: pillars underneath the nucleus and
2. $d > R_{nuc}$: pillars in the region surrounding the nucleus.

The size of radial deflections depended on the distance of the pillar-spots to the center of the nucleus (Fig. 4.8 - 4.9). In figure 4.8, the radial deflection versus the distance of the pillar/pillar-spots to the center of the nucleus is shown for single metaphase cells on stiff 47.2 kPa pillars and a 2.5 MPa flat layer. Both on the stiff micropillars as well as on the flat layer of PDMS, an upward trend was observed in the first regime. A downward trend was observed in the second regime. Equation 2.6 was fit to the data points in the first regime. The nucleus of the cell on the stiff pillars had radius $d < R_{nuc} = 8.77 \mu\text{m}$. The fit yields: $R = 8.75 \pm 0.15 \mu\text{m}$, $H = 9.6 \pm 0.9 \mu\text{m}$ and $n_1/n_2 = 0.954 \pm 0.011$. On the flat layer, the nucleus of the metaphase cell had a radius $d < R_{nuc} = 8.88 \mu\text{m}$. The fit resulted in $R = 8.8 \pm 1.0 \mu\text{m}$, $H = 9.6 \pm 1.7 \mu\text{m}$ and $n_1/n_2 = 0.96 \pm 0.02$. Within the error range, results of the two fits are comparable.

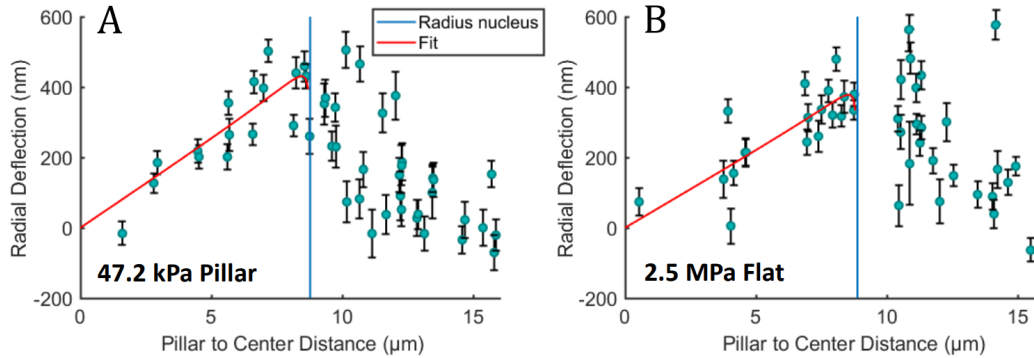


Figure 4.8: Refraction at a semi-spherical surface can describe the outward pointing deflections underneath the nucleus. **A.** Individual pillar deflection versus the distance from the center of the nucleus of a single metaphase cells on 47.2 kPa micropillars. The model described by eq. 2.6 was fit to the pillars underneath the nucleus, i.e. $d < R_{nuc} = 8.77 \mu\text{m}$ and is shown in red. It yields: $R = 8.75 \pm 0.15 \mu\text{m}$, $H = 9.6 \pm 0.9 \mu\text{m}$ and $n_1/n_2 = 0.954 \pm 0.011$. **B.** And a single metaphase cell on a 2.5 MPa flat layer of PDMS. The fit for $d < R_{nuc} = 8.88 \mu\text{m}$ yields $R = 8.8 \pm 1.0 \mu\text{m}$, $H = 9.6 \pm 1.7 \mu\text{m}$ and $n_1/n_2 = 0.96 \pm 0.02$. The errorbars show the inaccuracy in determining the center-point of the pillar-spots.

As shown in figure 4.9, combining data of multiple cells resulted in a similar trend. Radial deflections of 13 metaphase cells on stiff pillars and 16 metaphase cells on a stiff flat layer were combined in figure 4.9 A and B respectively. The same two regimes were distinguished, now taking into account the average size of the nuclei R_{av} :

1. $d < R_{av}$: pillars underneath the nuclei and
2. $d > R_{av}$: pillars in the region surrounding the nuclei.

The correlation coefficient for each individual trace was calculated for each regime (Fig. 4.9 C). On both the stiff micropillars as well as on the stiff flat layer of PDMS, a clear positive correlation was found for radial deflections of pillars underneath the nucleus. A clear negative correlation was found for the radial deflection in the region surrounding the nucleus. Equation 2.6 was fit to the data points in the first regime. On the stiff pillars, the average radius of the nucleus was $R_{av} = 8.47 \mu\text{m}$. The fit yields: $R = 8.5 \pm 0.4 \mu\text{m}$, $H = 9.3 \pm 0.5 \mu\text{m}$ and $n_1/n_2 = 0.954 \pm 0.007$. On the flat layer of PDMS the average radius of the nucleus was $R_{av} = 8.67 \mu\text{m}$. Fitting eq. 2.6 to the first regime yields: $R = 8.66 \pm 0.06 \mu\text{m}$, $H = 9.4 \pm 0.4 \mu\text{m}$

and $n_1/n_2 = 0.974 \pm 0.004$. Table 4.1 shows an overview of the fit results. Of the combined data, the correlation coefficient on the 47.2 kPa pillars was 0.75 for $d < R_{av}$ and -0.60 for $d > R_{av}$. On the Flat layer of PDMS the correlation coefficient in the first regime was 0.42, and in the second regime -0.51 .

Measurements on the 47.2 kPa pillars were performed over multiple cells on several micropillar arrays. The results of one of these micropillar array measurements (shown in figure S3 C) was excluded in figure 4.9, because cells showed a different behaviour compared to the other measurements. Each set of measurements is shown individually in figure S3. A fit to the data that also includes the excluded measurement is shown in figure S4.

On the soft 9.8 kPa micropillar array, no clear correlation was observed between the pillar-to-center distance and the pillar-deflection. The combined distance versus deflection curve is shown in figure S2. Nuclei were larger and more flattened compared to the stiffer substrates. Fitting results are included in the overview in table 4.1.

Table 4.1: Overview of the fitting parameters.

Stiffness	R_{av} (μm)	R (μm)	H (μm)	n_1/n_2
9.8 kPa Pillar	8.9	9.0 ± 1.4	8.7 ± 1.7	0.987 ± 0.008
47.2 kPa Pillar	8.47	8.5 ± 0.4	9.3 ± 0.5	0.954 ± 0.007
2.5 MPa Flat	8.67	8.66 ± 0.06	9.4 ± 0.4	0.974 ± 0.004

Both on the stiff pillars as well as on the flat layer, radial deflection of pillar-spots increased as pillars were closer to the edge of the nucleus which could be explained by a sphere-cap shaped lens. Pillars/pillar-spots outside the nucleus showed a decreasing trend.

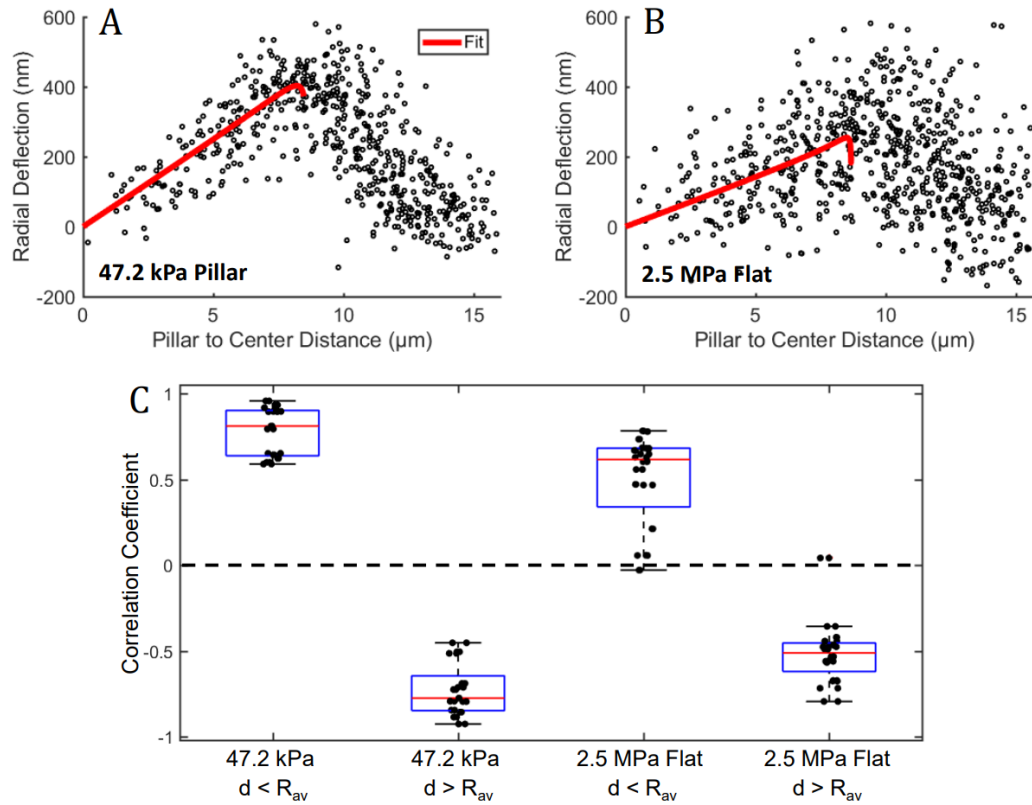


Figure 4.9: Deflections of pillar-spots underneath the nucleus increased as spots were further from the center. Pillars in the region surrounding the nucleus showed a decrease in deflection as the distance increased. A. Individual pillar deflection versus the distance from the center of the nucleus of a 13 metaphase cells on 47.2 kPa micropillars. The model described by eq. 2.6 was fit to the pillars underneath the nucleus, i.e. $d < R_{av} = 8.47 \mu\text{m}$, and is shown in red. It yields: $R = 8.5 \pm 0.4 \mu\text{m}$, $H = 9.3 \pm 0.5 \mu\text{m}$ and $n_1/n_2 = 0.954 \pm 0.007$. **B.** And 16 metaphase cells on a 2.5 MPa flat layer of PDMS. The fit for $d < R_{av} = 8.67 \mu\text{m}$ yields $R = 8.66 \pm 0.06 \mu\text{m}$, $H = 9.4 \pm 0.4 \mu\text{m}$ and $n_1/n_2 = 0.974 \pm 0.004$. **C.** Correlation between the distance d from the center of the nucleus and the deflection for pillars underneath the nucleus ($d < R_{av}$) and for the region surrounding the nucleus ($d > R_{av}$). Data points indicate the correlation coefficient of individual cells. On both substrates, a clear positive correlation was observed for $d < R_{av}$. A clear negative correlation was found for $d > R_{av}$.

Discussion

We hypothesized that outward deflections of micropillars during cell division were mainly caused by astigmatism. The results shown in this thesis strongly suggest that this is the case. On a flat, stiff, nondeformable layer of PDMS, for metaphase cells we found deformations in a μ -printed hexagonal pattern radially outward with respect to the center of the nucleus up to 400 nm. These findings are not limited by our measurement accuracy; they are a factor of four above our lower bound of 113 nm (Fig. 4.5). The highest outward deflections were measured during metaphase.

Outward deflections on the soft 9.8 kPa micropillars were lower compared to their stiffer counterpart. Cell behaviour is influenced by its environment. Previous studies have shown that cells spread more on stiffer substrates [15, 16]. We have two possible explanations on why we measured lower deflections on the soft pillars. Unlike what is shown in previous studies, our HeLa cells may spread more on the soft pillars, resulting a lens of lower strength. Another explanation is that cells are able to pull soft pillars inward, even during cell division. Real inward deflections the pillars would counteract the outward pseudo-deflections due to the lens effect.

Until now we did not consider a difference in refractive index between the cell medium and cytosol, while in reality they differ [9]. By accurately matching the refractive index of the cell medium to the refractive index of the cytosol as described by [17], the simple model could give a more accurate indication for the refractive index of the nucleus. Assuming that the cytosol only forms a thin film on top of nucleus, we can estimate the refractive index of the nucleus. The refractive index of the cell medium is $n_1 = 1.33$. Using the results from the fit in figure 4.9 then yields $n_2 = 1.366 \pm 0.004$ on for the refractive index of the nucleus. This value is

similar to the one found previously [9].

We saw that pillars/pillar-spots in the region surrounding the nucleus showed a decreasing trend in their radial deflection as they were further from the center of the nucleus (Fig. 4.9). The model introduced in chapter 2 does not capture this downward trend. The negative correlation for the deflections outside the nucleus, but inside the cell, could be explained by a change in the sign of the curvature of the interface (Fig. 5.1). Close to the boundary of the nucleus, the vertical distance light travels through cytoplasm is larger compared to the center of the cell. The curvature of the cell changes from convex to concave at this point. As the distance to the center then increases, the interface becomes more parallel to the substrate. Deflections then decrease with increasing distance. The exact deflection highly depends on the curvature, which we could not measure on our micropillar arrays.

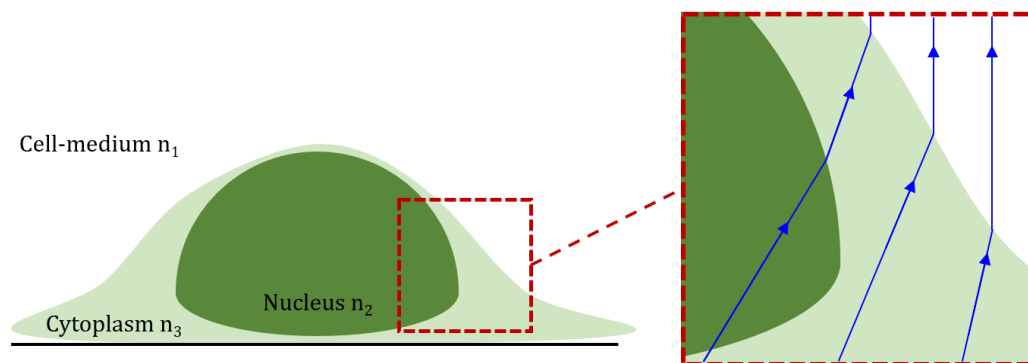


Figure 5.1: Negative correlation for pillars surrounding the nucleus in figure 4.9 could be explained by a change in the sign of the curvature of the cell medium - cell membrane interface. Lens effect caused by the nucleus increases towards the edge of the nucleus. The thin layer of cytoplasm barely influences the effect. As the curved edge of the nucleus becomes more perpendicular to the substrate, it is covered by a thicker layer of cytoplasm. The curvature of the cytoplasm-cell medium interface changes sign close to the edge of the nucleus. The interface between cell-medium and cell-membrane then gradually becomes more parallel to the substrate resulting in a decreasing trend in the deflection as the distance to the center of the nucleus increases.

Deflections up to 700 nm are not observed, even though predicted by eq. 2.7. Boundary effect, where also the cytosol plays a significant role, decreases the total deflection. As shown in figure 5.1, some light rays are refracted twice: first at the nucleus-cytoplasm interface, then at the cytosol-cell medium interface. In the case we overestimate the size of the

deflections; the actual deflections due to astigmatism are smaller than we expect.

As shown in figure 4.3, the increase in the net radial deflection could be explained by a shape change of the cell from flat to round. An increase in the refractive index of the nucleus would yield a similar result though. These changes in the refractive index during the cell cycle have been measured before, but only show fluctuations up to 0.005 [18]. Thus, this effect would only be a minor contribution to the overall radial deflection changes.

More accurate measurements on the shape of the cell itself could give further insight in the downward trend observed in figure 4.9. Optimizing the model introduced in chapter 2, such that it also covers refraction at the cell - cell medium interface could ultimately describe the whole curve in figure 4.9. This model could be used to differentiate between traction forces and astigmatism.

During traction force measurements, astigmatism should be taken into account, specifically when measuring forces close to the cell nucleus and especially in tightly packed cell-clusters.

Chapter 6

Conclusion

Cell-induced astigmatism in traction force measurements on micropillar arrays using super-resolution techniques [7] can result in aberrations up to 400 nm. Images of micropillar arrays, which are taken through the cell, are distorted by astigmatism caused by a refractive index change between the cell and cell-medium. Using a simple model that approaches the shape of the nucleus to that of a sphere-cap, we found that the refractive index of the nucleus is 1.366 ± 0.004 . Pushing forces during cell division, as measured previously by [8], are a merely a measurement artifact.

Acknowledgements

Special thanks to Julia Eckert for her guidance through the project and Prof.dr. Thomas Schmidt for giving me the opportunity to do this project. Thanks to Luise Herrmann and Radoslaw Gora for their valuable discussions.

Bibliography

- [1] O. Du Roure, A. Saez, A. Buguin, R. H. Austin, P. Chavrier, P. Siberzan, and B. Ladoux, *Force mapping in epithelial cell migration*, Proceedings of the National Academy of Sciences of the United States of America **102**, 2390 (2005).
- [2] B. Sabass, M. L. Gardel, C. M. Waterman, and U. S. Schwarz, *High Resolution Traction Force Microscopy Based on Experimental and Computational Advances*, Biophysical Journal **94**, 207 (2008).
- [3] M. Dembo and Y.-L. Wang, *Stresses at the Cell-to-Substrate Interface during Locomotion of Fibroblasts*, Biophysical Journal **76**, 2307 (1999).
- [4] U. Schwarz, N. Balaban, D. Riveline, A. Bershadsky, B. Geiger, and S. Safran, *Calculation of Forces at Focal Adhesions from Elastic Substrate Data: The Effect of Localized Force and the Need for Regularization*, Biophysical Journal **83**, 1380 (2002).
- [5] J. L. Tan, J. Tien, D. M. Pirone, D. S. Gray, K. Bhadriraju, and C. S. Chen, *Cells lying on a bed of microneedles: An approach to isolate mechanical force*, Proceedings of the National Academy of Sciences **100**, 1484 (2003).
- [6] P. Pandya, J. L. Orgaz, and V. Sanz-Moreno, *Actomyosin contractility and collective migration: may the force be with you*, Current Opinion in Cell Biology **48**, 87 (2017).
- [7] C. Coltharp and J. Xiao, *Superresolution microscopy for microbiology*, Cellular Microbiology **14**, 1808 (2012).
- [8] H. van Hoorn, *Cellular forces: adhering, shaping, sensing and dividing*, 2014.

-
- [9] W. Choi, C. Fang-Yen, K. Badizadegan, S. Oh, N. Lue, R. R. Dasari, and M. S. Feld, *Tomographic phase microscopy*, *Nature Methods* **4**, 717 (2007).
- [10] M. P. Stewart, J. Helenius, Y. Toyoda, S. P. Ramanathan, D. J. Muller, and A. A. Hyman, *Hydrostatic pressure and the actomyosin cortex drive mitotic cell rounding*, *Nature* **469**, 226 (2011).
- [11] H. Van Hoorn, R. Harkes, E. M. Spiesz, C. Storm, D. Van Noort, B. Ladoux, and T. Schmidt, *The nanoscale architecture of force-bearing focal adhesions*, *Nano Letters* **14**, 4257 (2014).
- [12] L. Trichet, J. Le Digabel, R. J. Hawkins, S. R. K. Vedula, M. Gupta, C. Ribault, P. Hersen, R. Voituriez, and B. Ladoux, *Evidence of a large-scale mechanosensing mechanism for cellular adaptation to substrate stiffness*, *Proceedings of the National Academy of Sciences* **109**, 6933 (2012).
- [13] G. Banfalvi, *Cell Cycle Synchronization*, *Methods in Molecular Biology* 761, Springer Science+Business Media, 2011.
- [14] D. Lehnert, *Cell behaviour on micropatterned substrata: limits of extracellular matrix geometry for spreading and adhesion*, *Journal of Cell Science* **117**, 41 (2004).
- [15] T. Yeung, P. C. Georges, L. A. Flanagan, B. Marg, M. Ortiz, M. Funaki, N. Zahir, W. Ming, V. Weaver, and P. A. Janmey, *Effects of substrate stiffness on cell morphology, cytoskeletal structure, and adhesion*, *Cell Motility and the Cytoskeleton* **60**, 24 (2005).
- [16] H. E. Balcioglu, L. Balasubramaniamb, T. V. Stirbatb, B. Dossa, M.-A. Fardinb, R.-M. Mègeb, and B. Ladoux, *A subtle relationship between substrate stiffness and collective migration of cell clusters*, *Soft Matter* (2020).
- [17] T. Boothe, L. Hilbert, M. Heide, L. Berninger, W. B. Huttner, V. Zaburdaev, N. L. Vastenhouw, E. W. Myers, D. N. Drechsel, and J. C. Rink, *A tunable refractive index matching medium for live imaging cells, tissues and model organisms*, *eLife* **6**, 1 (2017).
- [18] R. K. Bista, S. Uttam, P. Wang, K. Staton, S. Choi, C. J. Bakkenist, D. J. Hartman, R. E. Brand, and Y. Liu, *Quantification of nanoscale nuclear refractive index changes during the cell cycle*, *Journal of Biomedical Optics* **16**, 070503 (2011).

Supplementary Information

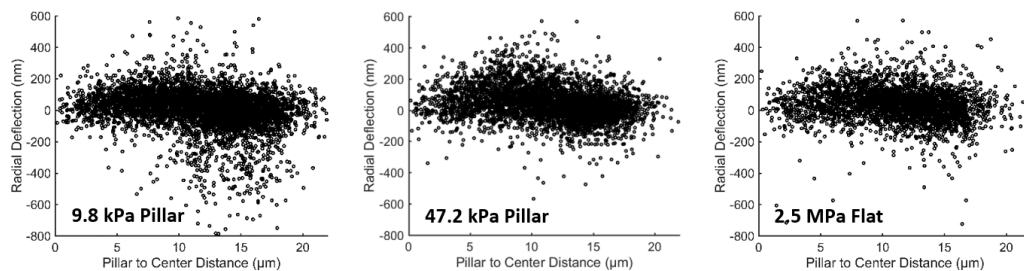


Figure S1: Interphase cells did not show clear outward radial deflections underneath the nucleus. A. 70 cells on 9.8 kPa pillars. Between 0 - 10 μm , deflections were distributed almost symmetrically around zero. Traction forces were observed between 10 - 20 μm from the center of the nucleus. **B.** 65 cells on 42.2 kPa pillars. A minor increase in deflections is seen between 0 - 10 μm , but this increase highly differed from cell to cell. A fewer amount of traction forces was observed compared to (A). **C.** 49 cells on a 2.5 MPa Flat layer. Deflections were distributed close to zero. Determining deflections of pillar spots was limited by the measurement accuracy.

Table S1: P-values resulting from a two-sided Wilcoxon rank sum test of the distributions of net tangential deflections.

	Interphase			Metaphase		
	9.8 kPa	47.2 kPa	2.5 MPa	9.8 kPa	47.2 kPa	2.5 MPa
Interphase	9.8 kPa	1	0.33	0.25	0.40	0.41
	47.2 kPa	0.33	1	0.8	1	0.8
	2.5 MPa	0.25	0.8	1	0.7	0.9
Metaphase	9.8 kPa	0.40	1	0.7	1	0.98
	47.2 kPa	0.47	0.8	0.6	0.8	0.8
	2.5 MPa	0.41	0.7	0.9	0.98	1

Table S2: *P-values resulting from a two-sided Wilcoxon rank sum test of the distributions of net radial deflections.*

	Interphase			Metaphase		
	9.8 kPa	47.2 kPa	2.5 MPa	9.8 kPa	47.2 kPa	2.5 MPa
Interphase	9.8 kPa	< 0.0001	< 0.0001	< 0.0001	< 0.0001	< 0.0001
	47.2 kPa	1	0.90	2.4e-03	< 0.0001	< 0.0001
	2.5 MPa	< 0.0001	1	8.3e-04	< 0.0001	< 0.0001
Metaphase	9.8 kPa	< 0.0001	8.3e-04	1	9.2e-04	0.017
	47.2 kPa	< 0.0001	< 0.0001	9.2e-04	1	0.38
	2.5 MPa	< 0.0001	< 0.0001	0.017	0.38	1

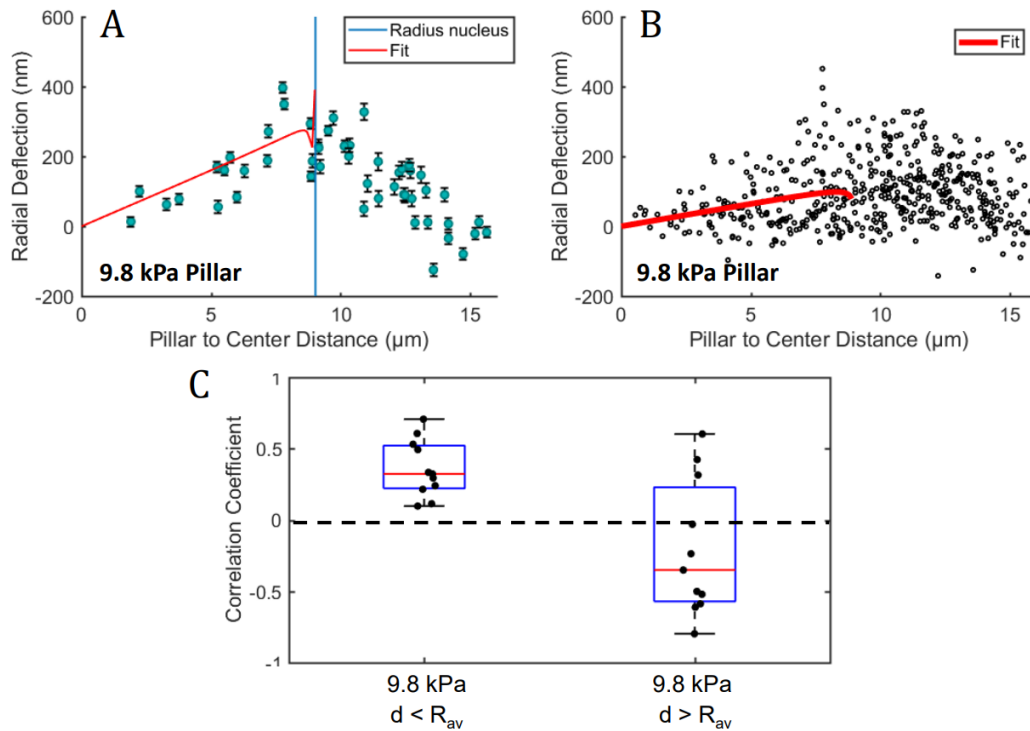


Figure S2: Radial pillar deflections of metaphase cells on a soft micropillars were lower compared to deflections on a stiff micropillar array. **A.** Individual pillar deflection versus the distance from the center of the nucleus of a single metaphase cells on 9.8 kPa micropillars. The model described by eq. 2.6 was fit to the pillars underneath the nucleus, i.e. $d < R_{nuc} = 9.0 \mu\text{m}$ and is shown in red. It yields: $R = 8.86 \pm 0.08 \mu\text{m}$, $H = 9.4 \pm 0.7 \mu\text{m}$ and $n_1/n_2 = 0.970 \pm 0.008$. The errorbars show the inaccuracy in determining the center-point of the pillar-spots. **B.** Individual pillar deflection versus the distance from the center of the nucleus of a 11 metaphase cells on 9.8 kPa micropillars. The model described by eq. 2.6 was fit to the pillars underneath the nucleus, i.e. $d < R_{av} = 8.9 \mu\text{m}$ and is shown in red. It yields: $R = 9.0 \pm 1.4 \mu\text{m}$, $H = 8.7 \pm 1.7 \mu\text{m}$ and $n_1/n_2 = 0.987 \pm 0.008$. **C.** Correlation between the distance d from the center of the nucleus and the deflection for pillars underneath the nucleus ($d < R_{av}$) and for the region surrounding the nucleus ($d > R_{av}$).

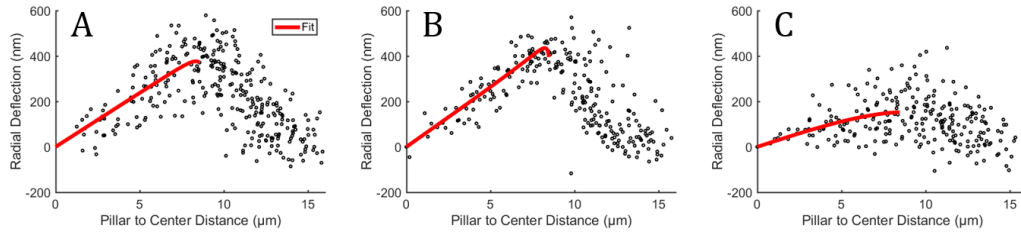


Figure S3: Measurements performed on 7 (A), 6 (B) and 6 (C) metaphase cells on different 47.2 kPa micropillar arrays under the same conditions showed different behaviour. A fit of eq. 2.6 to the pillars underneath the nucleus yields: A. $R = 9 \pm 2 \mu\text{m}$, $H = 9.3 \pm 0.9 \mu\text{m}$ and $n_1/n_2 = 0.955 \pm 0.017$. B. $R = 8.52 \pm 0.16 \mu\text{m}$, $H = 9.4 \pm 0.3 \mu\text{m}$ and $n_1/n_2 = 0.953 \pm 0.004$. C. $R = 17 \pm 93 \mu\text{m}$, $H = 7 \pm 21 \mu\text{m}$ and $n_1/n_2 = 0.9 \pm 0.6$.

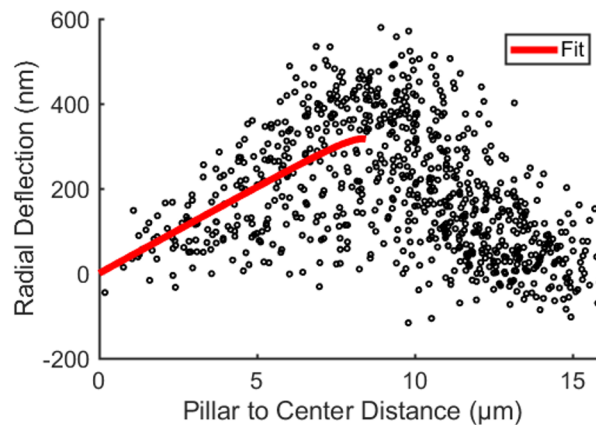


Figure S4: Using all measurement results in a wider spread of data points. Individual pillar deflection versus the distance from the center of the nucleus of a 19 metaphase cells on 47.2 kPa micropillars as shown separately in figure S3. The model described by eq. 2.6 was fit to the pillars underneath the nucleus, i.e. $d < R_{qv} = 8.46 \mu\text{m}$ and is shown in red. It yields: $R = 9 \pm 5 \mu\text{m}$, $H = 9 \pm 3 \mu\text{m}$ and $n_1/n_2 = 0.96 \pm 0.19$.